Optimizing the structure of Ni–Ni(OH)$_2$/NiO core-shell nanowire electrodes for application in pseudocapacitors: The influence of metallic core, Ni(OH)$_2$/NiO ratio and nanowire length

Pier Giorgio Schiavi, Pietro Altimari, Flavio Marzolo, Antonio Rubino, Robertino Zanoni, Francesca Pagnanelli

PII: S0925-8388(20)34082-2

DOI: https://doi.org/10.1016/j.jallcom.2020.157718

Reference: JALCOM 157718

To appear in: *Journal of Alloys and Compounds*

Received Date: 13 August 2020

Revised Date: 9 September 2020

Accepted Date: 23 October 2020

Please cite this article as: P.G. Schiavi, P. Altimari, F. Marzolo, A. Rubino, R. Zanoni, F. Pagnanelli, Optimizing the structure of Ni–Ni(OH)$_2$/NiO core-shell nanowire electrodes for application in pseudocapacitors: The influence of metallic core, Ni(OH)$_2$/NiO ratio and nanowire length, *Journal of Alloys and Compounds* (2020), doi: https://doi.org/10.1016/j.jallcom.2020.157718.

Pier Giorgio Schiavi: Conceptualization, Methodology, Data curation, Writing- Original draft preparation, Writing- Reviewing and Editing **Pietro Altimari**: Writing- Original draft preparation, Writing- Reviewing and Editing, Formal analysis **Flavio Marzolo**: Methodology, Data curation **Robertino Zanoni**: Methodology, Data curation, Investigation, Writing - Review & Editing. **Francesca Pagnanelli**: Supervision, Resources, Visualization

Optimizing the structure of Ni-Ni(OH)$_2$/NiO core-shell nanowire electrodes for application in pseudocapacitors: the influence of metallic core, Ni(OH)$_2$/NiO ratio and nanowire length

Pier Giorgio Schiavi*, Pietro Altimari*, Flavio Marzolo, Antonio Rubino, Robertino Zanoni and Francesca Pagnanelli

Department of Chemistry, Sapienza University of Rome, Piazzale Aldo Moro n.5, 00185, Rome, Italy

**correspondence concerning this article should be addressed to: piergiorgio.schiavi@uniroma1.it, pietro.altimari@uniroma1.it*

Abstract

An experimental analysis was performed to optimize the structure of Ni-Ni(OH)$_2$/NiO core-shell nanowire electrodes for improving their application in pseudocapacitors. Thickness and composition of the active phase shell were compared after thermal treatments at 40, 70 and 300°C. A Ni(0) core was found by XPS in the electrode treated at 40°C, it was still present after a temperature increase to 70°C but with a lower Ni(OH)$_2$/NiO ratio of the active phase shell, and disappeared after annealing at 300 °C, with a corresponding increase of the charge transfer resistance. The capacitance values increased from 40 to 70°C and drop to a minimum for the electrode treated at 300°C. A tailoring of the capacitance of the nanowire electrodes by controlling their length was evaluated. A constant capacitance per nanowires length unit was attained between 5 and 21 μm, indicating that the corresponding mass transfer resistance was negligible over the explored range. These results evidence the relevance to tightly control the thickness and ratio between the Ni(OH)$_2$ and NiO in the nanowires shell and provide a guideline to optimize the capacitance of the electrode by controlling the nanowire length.

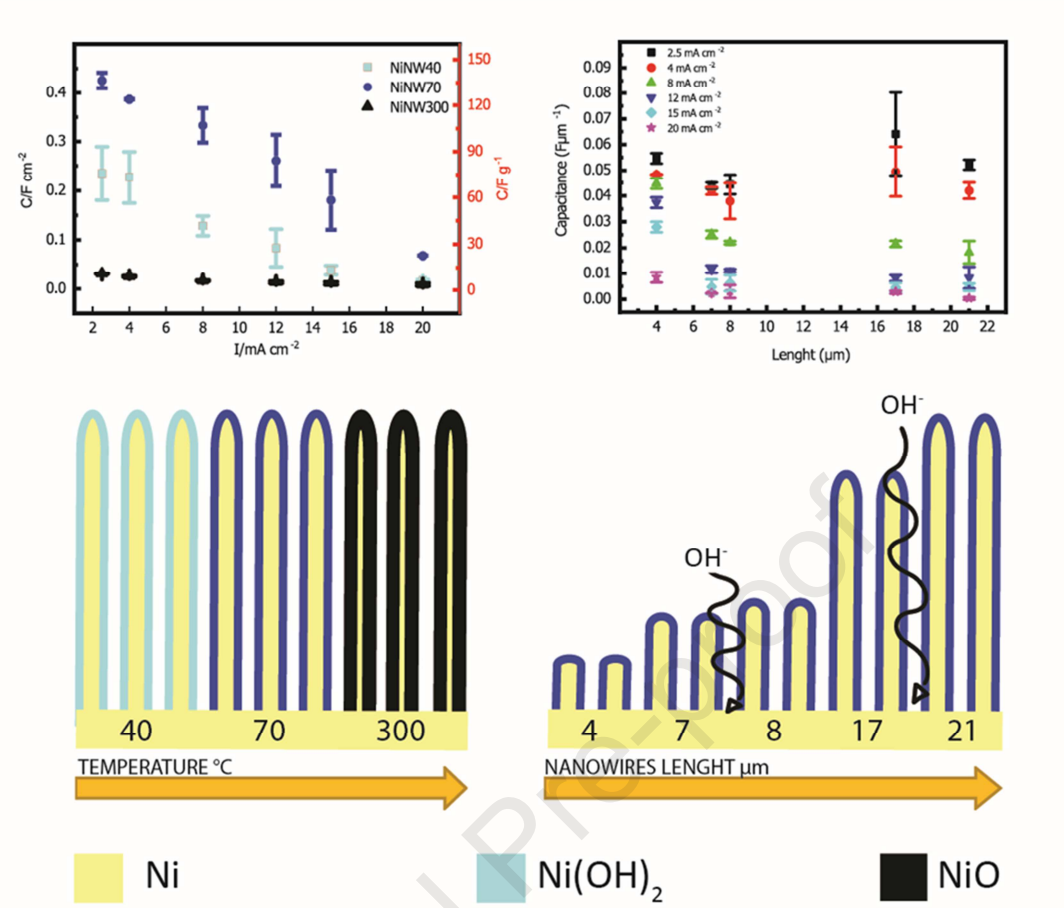

Graphical abstract

1. Introduction

The increase in the energy demand and the need to reduce the environmental impact of conventional energy production systems have motivated over the past decade an unprecedented interest of academics and industries towards the production of electric energy from renewable sources, including wind, solar and geothermic. These clean energy sources are recognized as a sustainable alternative to fossil fuels, but they are characterized by a discontinuous nature, making the development of reliable electric energy storage systems a crucial step towards the green energy transition [1, 2].

In this framework, electrochemical capacitors have attracted considerable attention due to their high-power density, long life cycling stability and fast energy delivery [3, 4]. However, electrochemical capacitors suffer from very low energy density (5-10 $Whkg^{-1}$), especially if compared with batteries (120-170 $Whkg^{-1}$) [5, 6]. In order to overcome this limitation, researchers have recently focused on the development of hybrid supercapacitors, which are composed of a pseudocapacitive electrode and capacitive-type electrode. With capacitive-type electrodes, energy storage is enabled by charge separation at the double layer forming at the electrode/solution interface. These electrodes are typically produced by employing high surface area carbonaceous materials to ensure satisfactory electric conductivity and high specific capacity [7, 8]. Differently, in the pseudocapacitive materials the energy storage is attained by both double layer formation at the solid/electrolyte interface and reversible fast redox reactions [9]. Pseudocapacitive materials thus merge the advantages of battery and purely capacitive-type materials. This allows improving the energy density as compared to purely-capacitive electrodes, ensuring at the same time energy delivery rates that may hardly be attained with only pseudocapacitive electrodes.

Noble metal oxides such as RuO_2 and IrO_2 are known as the most effective pseudocapacitive electrode materials, but the high cost and toxicity limit their application [9-12]. Transition metal oxides/hydroxides have been extensively studied due to their high specific capacitance and good cycling stability. In addition, synthesis methods have been developed allowing effectively controlling the morphology of transition metal oxides nanostructures and thus tailor the electrochemical performances to the targeted application objective [13-19]. Among the transition metals, Ni-based materials are the more attractive, which can be explained by their high theoretical capacitance, abundance, environment friendliness, and good thermal and chemical stability. Particularly, numerous studies have reported the application of NiO and $Ni(OH)_2$ materials in the production of supercapacitor electrodes (e.g. [20-25]). On the other hand, NiO and $Ni(OH)_2$ suffers from low

conductivity originating from their intrinsic semiconductor or insulator nature, which increases the overall resistance and limits the kinetics of faradaic conversion reactions. Further, swelling and shrinkage take place during the charge and discharge of NiO and $Ni(OH)_2$, owing to the different densities of the oxidized and reduced forms, which can hinder the cycling stability [20].

In order to improve the electrode conductivity, the coupling of NiO and/or $Ni(OH)_2$ to high conductivity materials has been exploited. The dispersion of NiO and $Ni(OH)_2$ over porous carbonaceous materials allowed improving the electronic conductivity, increasing, at the same time, the specific surface area [12, 26-31]. However, this strategy is limited by the large resistances at the interface between the active phase and the carbon materials and by the hydrophobic nature of carbon materials hindering the effective soaking of the electrolyte[32]. These obstacles can be overcome by the dispersion of the NiO and $Ni(OH)_2$ phases over metallic foams. An alternative converse voltage method leading to the formation of molecular structure with abundant defects, lattice disorders, and connecting holes, enhancing the performance of Co-based electrodes was recently published [33]. The approach commonly implemented includes the application of Ni foams. These are characterized by a reticular and porous structure (pore diameter~1 mm) yielding a specific surface ranging from about 10 to 100 m^{-1}. Therefore, the deposition of nanoporous NiO and $Ni(OH)_2$ nanostructures is imperative with nickel foams to increase the specific surface area between the electrolyte and the active phase and thus ensure satisfactory capacitance values (500–2500 $F g^{-1}$). To this purpose, the synthesis of disparate NiO and $NiOH_2$ nanoporous structures, including, for example, nanoparticles [34], nanoflakes [35] nanotubes [36] and nanowires [37] was evaluated.

An alternative strategy includes the direct growth of active material on metallic nanowire arrays standing over a conductive substrate [38, 39]. As compared to the aforementioned nickel foams, these nanowire electrodes exhibit a specific surface area order of magnitudes larger and they are characterized by a regular porous structure, which can enhance mass transfer. Nanowires can be either directly grown over a conductive substrate by hydrothermal synthesis [38] or they can be produced by electrodeposition into the nanopores of a template [40], the latter strategy ensuring improved control over the nanowire aspect ratio and length distribution [41]. In addition, the hydrothermal synthesis route typically yields metal oxide/hydroxide nanowires, thus requiring a thermal reduction to generate a metallic nanowires core, while metallic nanowires can be directly produced by template electrodeposition [38]. While a sufficiently thick nanoporous shell of the active phase need to be deposited over the surface of metallic nickel foams, the

considerably larger specific surface area of nanowire electrodes ensures that satisfactory capacitance values can be attained by introducing a few nanometres uniform shell, composed of $Ni(OH)_2$ and/or NiO, covering the nanowire metallic core.

Controlling the thickness and the composition of the active phase shell is pivotal to optimize the electrode performances. Increasing the shell thickness can increase the faradaic contribution to the capacitance but it decreases the electronic conductivity [42], while varying the ratio $NiO/Ni(OH)_2$ can significantly improve electrochemical performances as compared to pure NiO or $Ni(OH)_2$ active phases [43].

The strategy that is commonly implemented to control thickness and the composition of the active phase includes the thermal treatment of the electrodes. This strategy was extensively implemented to optimize the composition of the active phase in pseudocapacitors produced by dispersion of $Ni(OH)_2$ on porous carbonaceous materials and metallic foams. On the other hand, only few studies investigated the impact of thermal treatment on the performance of nickel nanowires electrodes. In addition, these studies exclusively focused on oxide nanowires produced by the hydrothermal route. No study has in contrast evaluated the impact of thermal treatment on the performances of nanowire electrodes produced by template electrodeposition, though electrodeposition can considerably simplify the nanowire synthesis and the thermal treatment as compared to the hydrothermal route [44].

It should be emphasized at this point that the optimization of the electrode performances by thermal treatment is invariably limited by the need to maintain an active phase shell thin enough to avoid charge transport limitations (e.g. electronic conductivity, proton transport through the hydroxide phase). An effective strategy that can be exploited to increase the electrode capacitance is increasing the thickness of the overall electrodes, which corresponds, for nanowire electrodes, to increase the nanowire length. This allows increasing the mass of the active phase without modifying the thickness of the active phase shell covering the nanowires. However, increasing the nanowire length increases the resistance to the transport of the redox species through the electrolyte solution and a threshold nanowire length may be found above which the specific electrode capacitance is decreasing with further increasing the nanowire length. Yet, no study has systematically investigated how this strategy can be effectively implemented to tailor the capacitance of nanowire electrodes.

In this article, an experimental study is presented analysing the influence of thermal treatment and nanowire length on the performance of nickel nanowires electrodes produced by template electrodeposition. In order

to overcome the limitation of traditional template electrodeposition dictated by the growth of nanowires over an insulating substrate, a technique recently developed in our group was implemented. This includes uniformly growing the metallic nanowires until the alumina nanopores are completely covered by a thin metallic film. Alumina can then be selectively dissolved leaving a nanowire array standing over a thin metallic plate, which can work as current collector. Nanowire electrodes produced by this technique were treated at different temperatures in water (at 40 and 70 ^{o}C) and air (300 ^{o}C) and then evaluated for the application as positive electrodes in pseudocapacitors. Finally, the possibility to tailor the capacitance of the nanowire electrodes by controlling the nanowire length during the electrodeposition is analysed.

2. Experimental Section

2.1 Electrodes synthesis

The nickel nanowire electrodes (NiNW) were synthesized by an electrochemical method previously developed by the authors (see refs. [44, 45] for a detailed description including a schematic of the method). Nanowires were synthesized by electrodeposition into the nanopores of an alumina template generated by one-step anodization of low-purity aluminium. Electrodeposition was performed in a magnetically stirred three-electrode jacketed glass cell at constant temperature of 35 ± 0.2 °C. A 25×20 mm graphite foil, Ag/AgCl saturated electrode and the anodic alumina template with exposed area of 1.3 cm^2 were used as counter, reference and working electrode, respectively. The electrodeposition bath employed to perform the electrodeposition was a diluted nickel Watts bath with 30 gL^{-1} $NiSO_4$ $7H_2O$, 45 and 45 gL^{-1} H_3BO_3. The electrodeposition was performed by applying a constant voltage signal of -8 V vs Ag/AgCl for 100 ms and then the current was kept at zero for 2000 ms. These two pulses were repeated until the alumina nanopores were filled. A second electrodeposition was then performed to deposit a thin nickel film, which worked as current collector, over the filled alumina template by. This second electrodeposition was performed under the same conditions of nanowire electrodeposition but an electrolytic bath with 300 gL^{-1} $NiSO_4$ $7H_2O$ was used. The second electrodeposition was carried out until transferring a charge of 60 C, which yielded a nickel film of about 6 μm. Finally, alumina and aluminium were completely removed by selective etching in NaOH 6 M at 40°C and 70°C. Hereafter, electrodes produced by etching at 40 and 70^{o}C are referred to as NiNW40 and NiNW70, respectively. An additional electrode, referred to as NiNW300, was obtained by annealing in air the nanowire electrode at 300°C for 1h.

2.2 Electrode characterization

Field emission scanning electron microscopy (SEM, Zeiss Auriga) was employed to characterize the morphology and size of NiNW electrodes. Focused ion beam (FIB, Orsay Physics Cobra Ga column) was used to generate electrode cross sections. The chemical composition of the electrodes was determined by energy dispersive X-ray spectroscopy (EDX, Bruker QUANTAX 123 eV). The surface atomic composition of samples was analysed by X-ray Photoelectron Spectroscopy (XPS, Omicron NanoTechnology modified M-XPS system). The spectra were excited by Mg Kα photons (hv= 1253.6 eV) and monochromated Al Kα photons (hv= 1486.7 eV). Experimental spectra were theoretically reconstructed by a curve fitting procedure making use of symmetric pseudo-Voigt functions (linear combinations of pure gaussian and pure lorentzian peaks) and iteratively fitting the background to a Shirley or a linear function. XPS atomic ratios (given with ±10% associated error) between relevant core lines were calculated from experimentally determined area ratios corrected for the corresponding theoretical cross sections [46] and for a square root dependence of the photoelectrons kinetic energies. The samples were conductive and did not need energy scale corrections, as verified by the correspondence, within the associated experimental error, of Ni 2p energy position for metallic Ni in samples NiNW40 and NiNW70 with the corresponding data reported in the literature [47] and by the overlapping of O 1s peaks among all three samples NiNW40, NiNW70 and NiNW300.

2.3 Electrochemical characterization

The electrochemical characterization of the synthesized electrodes was performed by cyclic voltammetry (CV), galvanostatic cycling (GC) and electrochemical impedance spectroscopy (EIS) experiments. All the experiments were carried out using a three-electrode jacketed glass cell at constant temperature of 25°C. Ag/AgCl, platinum spiral and the NiNW electrode with an exposed area of 0.5 cm^2 were the reference, counter and working electrode, respectively. A KOH 1M electrolyte solution was employed. CVs were performed at scan rates of 10, 20, 50, 100, 200 mV/s, while GCs were performed at constant current density of 2, 4, 8, 12, 15, 20 mA/cm^{-2} within a potential range of 0-0.4V. EIS was performed in the 40 kHz–1 Hz frequency range, using 5 mV amplitude AC pulse. All the specific capacitance values reported throughout the manuscript were computed by using the total electrode weight, which includes the weight of the active

phase (Ni oxide/hydroxide) constituting the external shell of the nanowires and the weight of the nickel film used as current collector.

3. Results and discussion

SEM cross-sectional images of the nickel nanowires electrodes treated at different temperatures are shown in Figure 1. Low magnification images (Fig.1-A-B-C) did not evidence any significant difference between the electrodes treated at 40°C and 70°C (NiNW40, NINW70). With both these two latter electrodes, a compact and ordered nanowires array with a thickness of about 4 μm was found. Differently, irregularly shaped nanowires and a non-uniform distribution of the nanowire length across the array were evidenced by SEM analysis of the electrode treated at 300°C (NiNW300). This can be attributed to the formation of oxidized species, which can lead to a change in the nanowire volume. High magnification SEM images (Fig.1-D,E,F) evidenced the presence of irregular flakes on the surface of the NiNW40 electrode. These structures are typically formed during nickel electrodeposition owing to the concurrent precipitation of nickel hydroxide induced by local pH increase. This pH increase can be determined during the nickel electrodeposition by the hydrogen evolution reaction [48]. In this respect, it should be remarked that the electrodeposition method that was implemented to fill the alumina template involves the application of cathodic potentials allowing for water the electrochemical reduction on the nanowire surface [49, 50].

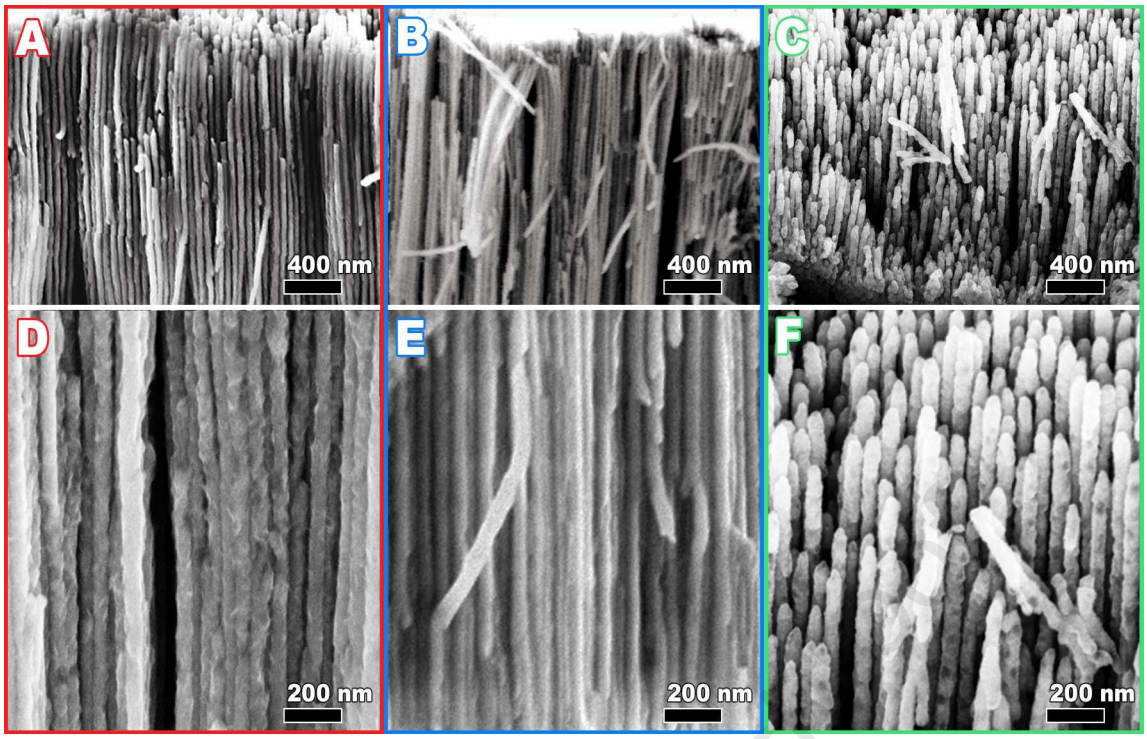

Figure 1: SEM cross-sectional images of the Ni NWS electrodes treated at 40 °C (A, D – red border), 70°C (B, E – blue border) and 300°C (C, F – green border).

Table 1. Electrodes composition [at.%] obtained from EDX and XPS analysis.

Electrode	EDX [at%]		XPS [at%]			
	Ni	O	Ni^0	NiO	$Ni(OH)_2$	Ni^0/Ni^{2+}
NiNW40	84.3	15.7	19.9	3.4	76.6	0.25
NiNW70	84.5	15.5	22.8	22.8	54.3	0.29
NiNW300	69.5	30.5	-	66.7	33.3	-

Electrode bulk and surface compositions were respectively characterized by EDX and XPS analysis. Bulk and surface atomic percentages of Ni and O measured with these two methods are reported in Table 1 (no trace or negligible percentages were found for all the other elements present in the electrolytic bath and the substrate).

3. (Table 1). For both Ni and O, identical bulk atomic percentages were found in the NiNW40 and NiNW70 electrodes. However, as compared to these two latter electrodes, an O atomic percentage twice larger was

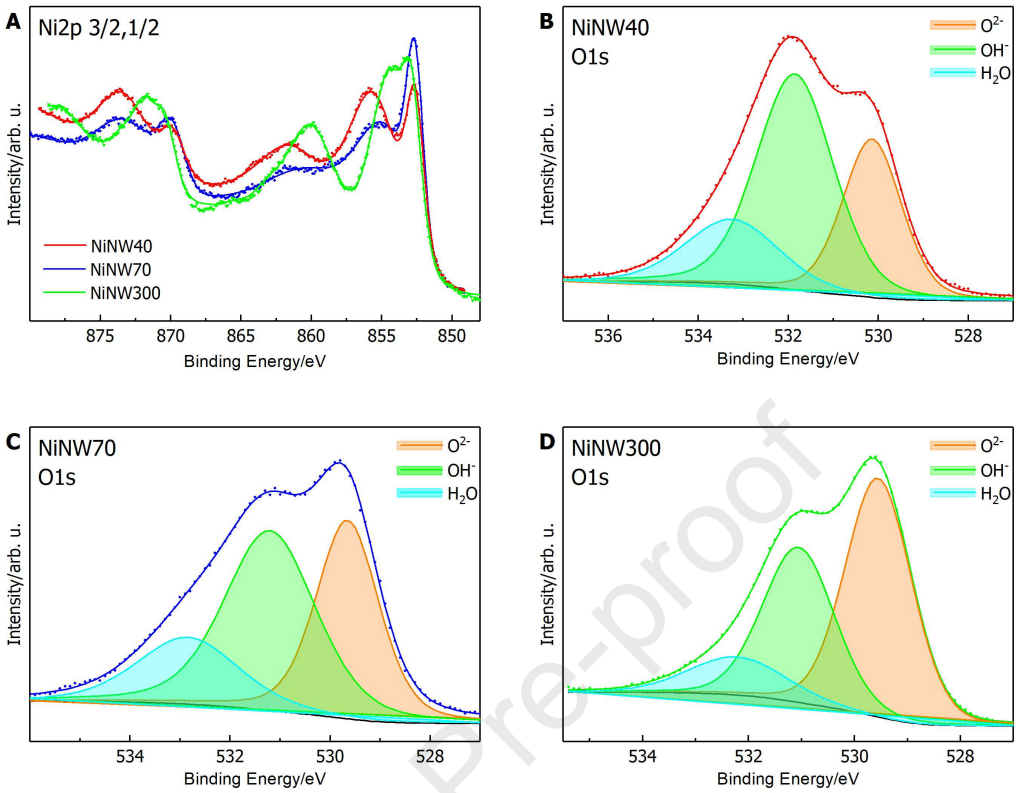

Figure 2. Ni 2p3/2,1/2 photoemission spectra of NiNW40-70-300 electrodes (A). O1s photoemission regions of NiNW40 (B), NiNW70 (C) and NiNW300 (C).

found by EDX in the NiNW300 electrode. In order to assess in-depth the surface composition of the NiNW40, NiNW70 and NiNW300 electrodes, angle-dependent XPS measurements were conducted by recording spectra at progressively more grazing angles. At the two extreme values (53 and 83°), the calculated escape depths are 1.5 and 0.30 nm for metallic Ni, [51] 1.7 and 0.35 nm for NiO, and 2.6 and 0.52 nm for oxygen [52]. The three samples showed substantial differences as a result of the distinct treatment undergone by each of them. A comparison among the Ni 2p photoemission regions taken at 53° from the three samples is displayed in Figure 2-A and at% values are reported in Table 1, while the curve fitting of Ni 2p spectra are collected in SI (Figure S2). The most evident difference resulting from Ni 2p peaks is the presence of a narrow component at low binding energy (BE) for samples NiNW40 and NiNW70, which is absent in NiNW300. This distinctive feature is further reflected in the Ni Auger spectrum (Figure S1), where again the NiNW300 lineshape is largely different from the other two, both of which present a sharp maximum peak at ~845 eV (kinetic energy scale), characteristic of metallic Ni. It is also evident how the Ni 2p lineshape of sample NiNW300 is indeed unique in the series, since its maximum, located at ~854 eV, is not reproduced

by either two samples. By comparison with relevant XPS literature [52, 53], sample NiNW300 only presents Ni(II) oxide/hydroxide species, which are present in NiNW40 and NiNW70 samples in addition to a metallic Ni component. The assignment comes from the lineshape and BEs of Ni2p and Auger lines. The nature of the Ni(II) species has been obtained by analysis of the O 1s region, displayed in Figure 2-B-C-D, and confirmed by a comparison with literature reports. In fact, O 1s is a complex region, where three components are immediately evident. In the full series, the peak envelope reveals, after curve-fitting, the presence of oxide and hydroxide plus chemisorbed water, at different relative amounts. Table 1 resumes the relevant quantitative ratios among Ni $2p_{3/2}$ and O 1s peak components, showing how the surface composition of the three samples can be somehow simplified into a Ni-$Ni(OH)_2$ electrode (NiNW40), a NiO electrode (NiNW300) and an intermediate case (NiNW70). Remarkably, XPS angle-dependent measurements (Fig.S2), have disclosed the core-shell nature of the nanowires. In fact, passing from 53° to 83°, samples NiNW40 and NiNW70 show the presence of a terminating layer of $Ni(OH)_2$ over an inner NiO deposit, the latter being grown on metallic Ni. With reference to the escape depth for metallic Ni at 83°, we can infer that the thickness of the oxide layer formed by NiO and $Ni(OH)_2$ is lower than 0.30 nm. Referring to the escape depth for metallic Ni at 53°, the thermal oxidation at 300°C produces an outer layer predominantly composed of NiO with a thickness higher than at least 1.50 nm. A final remark concerns the angle-dependent behaviour of the Ni 2p peak, where it is clear how the surface composition significantly varies only in the case of the NiNW40 sample, for which an intensification of the hydroxide-related component is shown in Figure Fig.S2.

In order to evaluate the capacitive characteristics of the produced electrodes, cyclic voltammetry experiments were carried out. Figure 3 and Fig.S3 present the cyclic voltammetry curves recorded with the fabricated nanowire electrodes at different scan rates. In all the reported curves, cathodic and anodic redox peaks can be clearly distinguished indicating that Faradaic processes significantly contribute to determine the electrode capacitance. The redox peaks can be associated to the following two main reversible reactions [54]:

$$NiOOH + e^- \leftrightarrows NiO + OH^- \quad (1)$$

$$NiOOH + H_2O + e^- \leftrightarrows Ni(OH)_2 + OH^- \quad (2)$$

NiNW40, NiNW70 and NiNW300 exhibit redox peaks over the same potential range.

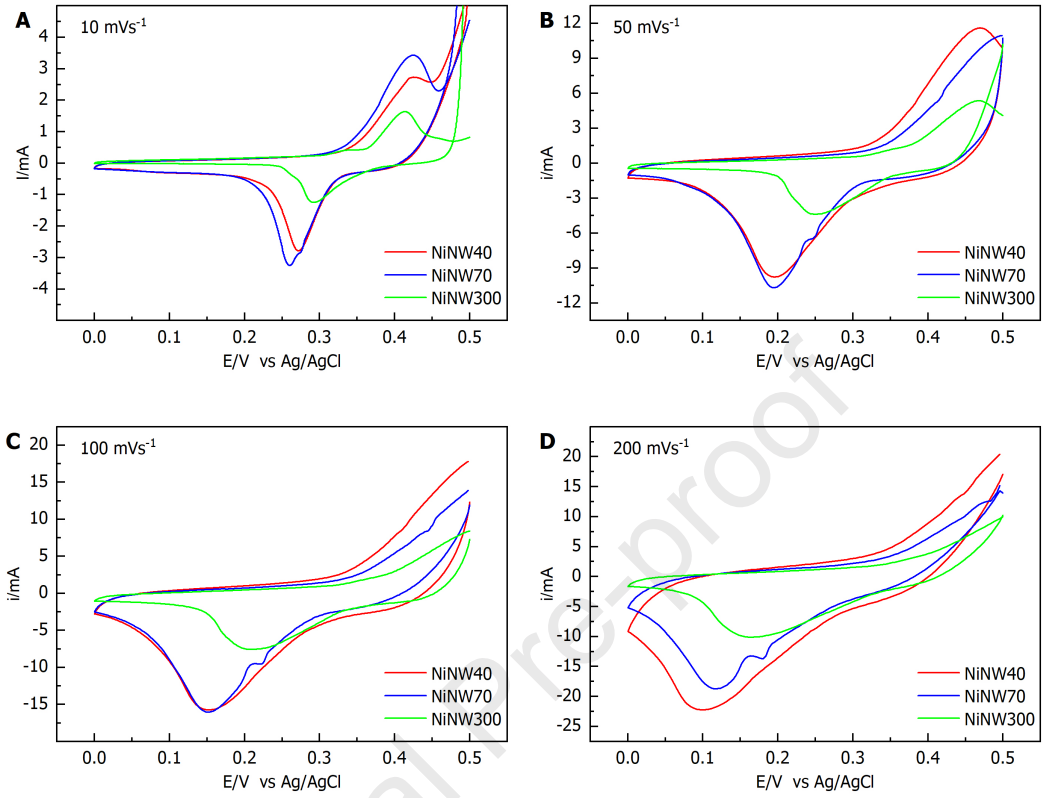

Figure 3: Cyclic voltammery curves of NiNW40, NINW70 and NiNW300 at various scan rates in 1 M KOH.

The wider cathodic peak arising at ~0.21 V can be attributed to the reduction of NiOOH to Ni(OH)2 (Eq. (2)), while the smaller cathodic peak at ~0.18 V can be imputed to the conversion to NiO. In the CV of the NiNW40 electrode, only the peak around 0.21V is detected, evidencing that the contribution of the oxidation to NiO is absent or negligible. As the temperature treatment is increased, with the NiNW70 electrode, a peak corresponding to the oxidation to NiO arises besides the wider cathodic peak at 0.21V determined by the formation of the Ni(OH)2 phase. Finally, with increasing the temperature to 300 oC, the peak at 0.21V corresponding to the formation of the Ni(OH)2 becomes barely distinguishable, suggesting that charging and discharging proceed by oxidation to NiOOH and successive exclusive formation of the NiO phase, which is evidenced by the peak at ~0.18V. The two identified cathodic peaks shift to lower potential values (i.e. more cathodic) with increasing the scan rate (Fig.3B-D), indicating that the electrode discharging process is governed at sufficiently cathodic potentials by diffusion.

During the anodic scan of any electrode, at the lowest scan rate (Fig.3A), a peak can be clearly identified around 0.4V, which can be imputed to the formation of NiOOH by oxidation of $Ni(OH)_2$ and NiO. Further increasing the potential beyond this peak, a current rise is determined around 0.45V by the oxidation of OH^-, i.e. by the oxygen evolution reaction (OER), catalysed by the oxidized Ni species [55, 56]:

$$4\,OH^- \rightarrow O_2 + H_2O + 4e^- \quad (3)$$

As the scan rate is increased (Figs.3B-D), the NiOOH oxidation peak shifts to larger potentials, which can be imputed to the limitations determined by proton diffusion through the electroactive phase NiOOH for Eq.2 and OH^- diffusion from NiOOH to the bulk electrolyte for Eq.1 [42]. With increasing the scan rate, the anodic peak eventually reaches the upper limit of the investigated potential window, thereby overlapping with the current rise generated by the O_2 evolution reaction. This latter reaction takes place at potential values close to the upper limit of the potential window (~0.45V), which is evidenced by the sharpt Remarkably, the potential value at which the OER is found to start in Fig. 3 is very close to the best value reported by recent electrocatalysis studies [57, 58], suggesting that the proposed electrode structures may configure a competitive OER electrocatalyst. A detailed evaluation of this application would then deserve to be investigated by separate studies.

Figure 4-A displays the capacitance computed from the cyclic voltammetries recorded at different scan rates by using the following formula:

$$C = \frac{1}{\nu\,\Delta E\,M}\int_{E_c}^{E_a} i(E)dE \quad (4)$$

where ν is the scan rate, ΔE is the potential window, i is the current, E_a and E_c are the start and the end potential of the cyclic voltammetry, respectively, and M is the total weight of the electrode or the geometric surface depending on whether the specific or the areal capacitance is computed, respectively. In accordance with Eq. 4, the capacitance is proportional to the area enclosed by the CV curve (Eq.4). By the application of Eq. 4, it was found that the capacitance increases with increasing the temperature of the treatment in water from 40 (NiNW40) to 70°C (NiNW70) (Fig.4-A-B), while a much lower capacitance value was found for the

by thermal treatment in air at 300 °C (NiNW300). This result was partly unexpected in what temperatures around 300 °C are typically adopted to maximize the capacitance of nickel electrodes [42].

It is important to remark that, as compared to the NiNW40 and NiNW70 electrodes, the NiNW300 electrode was characterized by a larger NiO content (Tab.1), which is in agreement with literature data. Particularly, previous studies evidenced that $Ni(OH)_2$ is progressively dehydrated with increasing the temperature up to 200-250 °C, while transition from $Ni(OH)_2$ to NiO takes place around 300 °C [42]. The lower capacitance attained, in contrast with the results reported by previous studies, with the NiNW300 electrodes may be then explained by the following mechanisms:

- Increased thickness of the external nickel oxide shell generated by the treatment at larger temperature. Since the diameter of the nanowire is not significantly varying during the thermal treatment, increasing the thickness of the oxide shell implies that the metallic Ni core becomes thinner, which increases the electrical resistance. The XPS analysis corroborates this hypothesis evidencing, for the NiNW300 electrode, a lack of the metallic Ni core as compared to the NiNW40 and NiNW70 electrodes.
- The bulk NiO contributes negligibly to the capacitance owing to the large resistance of OH- diffusion into NiO [42]. Therefore, thickening the NiO phase beyond a very thin layer covering the nanowire surface can only deteriorate the electronic conductivity without increasing the faradaic contribution to the capacitance.
- Oxide formation taking place during the nanowire thermal treatment is accompanied by swelling, which can decrease the specific surface area of the electroactive phase and generate, at the same time, structural defects compromising the electrical contact with the underlying metallic nickel. These effects become more relevant as the nanowire thickness undergoing oxidation is increased.

The above detailed mechanisms can decrease the current density recorded during the CV (Fig.3), ultimately resulting in a reduced electrode capacitance (Eq. 4). In order to quantify the impact of the metallic core thinning, EIS experiments were performed with the produced electrodes. Figure 4 shows the Nyquist plots of the different electrodes. Electrodes spectra can be described by the equivalent circuit model $R_e(R_{ct}W)(C_{dl})C_p$ (Fig.4-B), where R_e is the combination of ionic and electronic resistances, intrinsic resistance of the electrodes and contact resistance at the electrode/current collector interface, R_{ct} is the charge transfer resistance related to the electroactive surface area of the electrode, C_{dl} is the double layer capacitance, C_p is

the pseudo-capacitance, and W is the Warburg impedance [54, 59]. No significant difference was found between the model parameter values estimated for the electrodes NiNW40 and NiNW70 by fitting to EIS data (Table S1). R_e and R_{ct} varied from to 8.01 and 0.22 Ω, respectively, for the NiNW40 electrode, to 7.97 and 0.23 Ω, respectively, for the NiNW70 electrode. A significantly larger R_e, equal to 9.89 Ω, was found, in contrast, for the NiNW300 electrode, which can be explained by the increased thickness of the external oxide shell.

It is also important to notice that, in the EIS plot of any electrode (Fig.4-B), a linear branch arises over the mid-low frequency region, which marks the transition to diffusion control of the redox reactions (Eqs.1-2). The

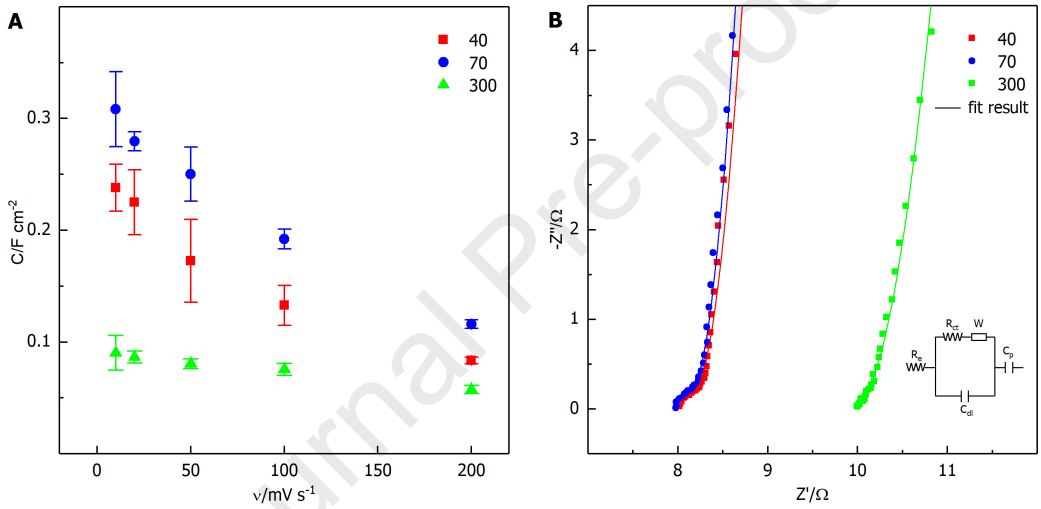

Figure 4: A) Capacitance values obtained from cyclic voltammetry experiments carried out at different scan rates. B) Nyquist plot recorded for the different electrodes. Inset the equivalent circuit model employed for the fitting of the experimental curves

EIS plot of the NiNW300 electrode is characterized the lowest slope of the linear branch, which reflects into the highest W impedance (Tab. S1). This difference can be partly explained by the increased diffusion of the OH^- into the NiO of the NiNW300 electrode, as compared to the diffusion of the proton into the $Ni(OH)_2$. Nonetheless, in accordance with XPS characterization, the differences between the diffusion resistances of the three electrodes could be also justified by the differences in the amounts of chemisorbed water. It is well known that diffusion in hydrated electrodes can occur by hopping of OH^- and H^+ through water molecules. Accordingly, increasing the amount of chemisorbed water is expected to enhance the diffusion through the electroactive phase [60]. As it can be inferred from Figure 2, the NiNW300 electrode exhibits the lowest amount of chemisorbed water.

However, the illustrated EIS analysis cannot sufficiently explain the (statistically) significantly larger capacitance of the NiNW70 electrode as compared to the NiNW40 electrode, nearly identical EIS spectra being recorded for these two electrodes (Fig.4). At this point, it is important to remark that, in accordance with XPS analysis, the electroactive phase of the NiNW70 electrode is characterized by the presence of both the NiO and the $Ni(OH)_2$ phases, while it is mainly composed of $Ni(OH)_2$ in the NiNW40 electrode. Previous studies evidenced that composite $NiO/Ni(OH)_2$ electrodes can exhibit capacitances larger than electrodes with pure active phases, i.e. either NiO or $Ni(OH)_2$ [43]. This was justified by the difference of the electron transfer during the faradaic reactions of NiO and $Ni(OH)_2$[43]. An alternative explanation could be a modification of the nanowire surface induced by the partial conversion of $Ni(OH)_2$ to NiO at 70°C. At this temperature, the active phase layer is sufficiently thin to maintain the metallic Ni core and the formation of the NiO phase is accompanied by the appearance of surface redox sites not present in the NiNW40 electrode, which can directly react with the OH^- to form the NiOOH phase. Since the bulk NiO does not contribute to capacitance, the partial conversion of $Ni(OH)_2$ to NiO is expected to be effective only if it covers a thin layer close to the external nanowire surface, which is the case of the NiNW70 electrode.

Galvanostatic cycling experiments were performed to evaluate electrode performances under varying charge-discharge rates. The evolution of the potential during cycling at different current densities is reported in Figure 5-A-B and Fig. S4. Charging for the electrodes NiNW40 and NiNW70 at the lowest current density of 2.5 mA cm^{-2} above 0.45V determines a constant potential profile, which can be explained by the OER Eq.3. In order to minimize the contribution of this reaction, the potential range was then restricted as compared to the cyclic voltammetry experiments to 0-0.4 V.

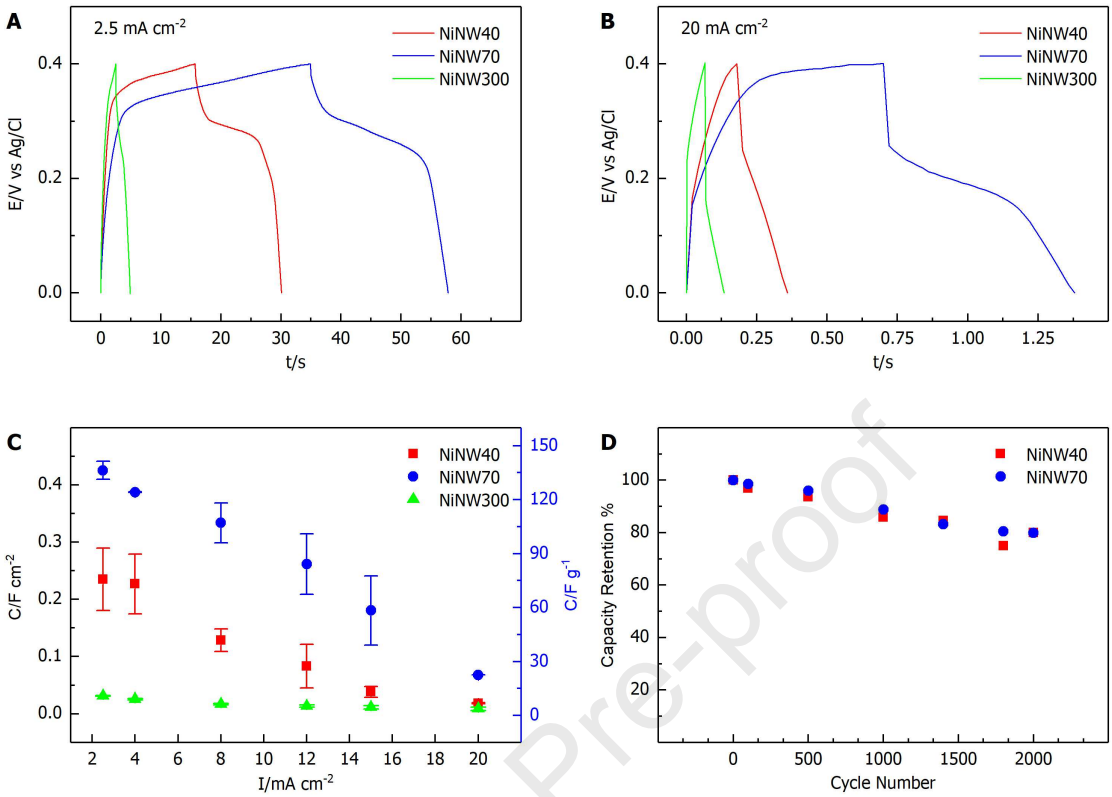

Figure 5: Charge–discharge curves at 2.5 mA cm^{-2} (A) and 20 mA cm^{-2} (B). C) Obtained capacitance from galvanostatic charge-discharge at different current densities. D) Capacitance retention of the NiNW40 and NiNW70 electrodes at 20 mA cm^{-2}

For any electrode, a non-linear potential profile was recorded during cycling, with plateaus appearing around the potential values corresponding to the reduction and oxidation peaks identified by cyclic voltammetry. In particular, the sharp linear increase and decrease of the potential can be attributed to double layer charge and discharge (double-layer capacitance contribution), respectively, while the potential plateaus are determined by the redox reactions Eqs. 2-3 (pseudocapacitance contribution). Capacitances were calculated from the galvanostatic cycling data by using the following formula:

$$C = \frac{i\,\Delta t}{\Delta E\; M} \qquad (5)$$

where i is the discharge current, Δt is the discharge time, ΔE is the potential window during the discharge and M is the total weight of the electrode or the geometric surface depending on whether the specific or the areal capacitance is calculated, respectively. The evolutions of the capacitance values with the current density for the three different electrodes are reported in Figure 5C. The capacitance follows a non-monotonic dependence on the treatment temperature. In agreement with the results of cyclic voltammetries, at any

current density, the capacitance increases with increasing the treatment temperature in water from 40 (NiNW40 electrode) to 70 °C (NiNW70 electrode) and then drops to a minimum with the NiNW300 electrode. These results clearly evidence the relevance to tightly control the ratio between the $Ni(OH)_2$ and NiO active phases. The higher capacitance attained by decreasing the $Ni(OH)_2$/NiO ratio in the NiNW70 electrode can be explained by the different charge transport mechanisms for $Ni(OH)_2$ and NiO. Charge transport with nickel hydroxide active phase involves the intercalation and diffusion of H^+ through the active material bulk. During charging, H^+ ions belonging to the $Ni(OH)_2$ phase combine at the electrode/electrolyte interface with the hydroxyl ions in solution to generate NiOOH and electrons. The electrons migrate through the active material to the current collector, while H^+ ions diffuse from the bulk of the $Ni(OH)_2$ phase (via solid state diffusion) to the electrode/electrolyte interface. On discharge, these processes are reversed, with the NiOOH reacting with water at the solid/electrolyte interface to extract H^+ ions, which diffuse from the solid-electrolyte interface to the bulk active material, thus converting NiOOH to $Ni(OH)_2$ [61]. Differently, the nickel oxide active phase reacts with OH^- ions mainly at sites distributed over the active material surface, with negligible contribution from OH^- diffusion into the material bulk [42, 62, 63].

In order to evaluate the stability of NiNW40 and NiNW70, charge-discharge galvanostatic cycling were performed at 20 mA cm^{-2} and up to 2000 cycles. Figure 5-D shows the capacitance retention trend over successive cycles. After 2000 continuous charge−discharge cycles, both the NiNW40 and NiNW70 electrodes retain the 80% of the initial capacity. This excellent result can be imputed to the structure of the nanowires array, which allows effectively accommodating the swelling and shrinkage of the active phase taking place during conversion reactions, thus ultimately preventing the capacity fading [64, 65]. This higher capacitance retention could pave the way to the application of the produced electrode in supercapacitors.

Influence of the nanowire length

The analysis illustrated in the previous section evidences that an optimal structure exists (thickness, composition), which can be attained by thermal treatment. Once such an optimal structure is attained, the only way to increase the electrode capacitance is to increase the nanowire length. Increasing the nanowire length can increase the mass of the electroactive phase leaving unchanged the active phase layer covering the nanowires.

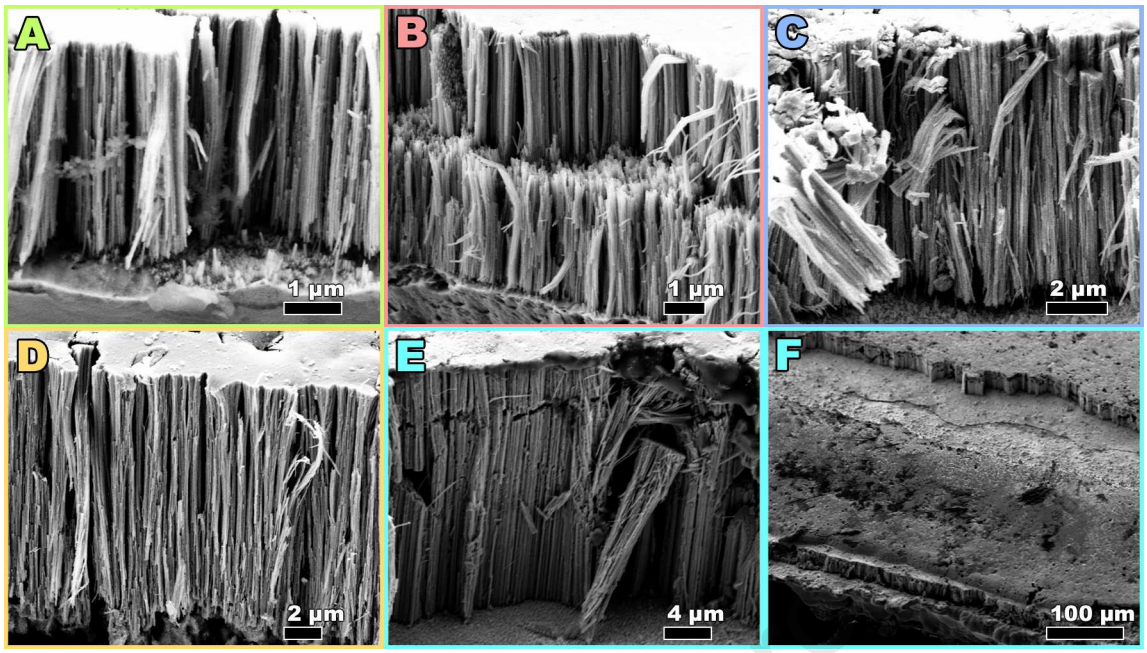

Figure 6: SEM cross-sectional images of the NiNW obtained by electrodeposition using alumina template produced with different anodization times 2 h (A), 3 h (B), 4 h (C), 8 h (D), 10 h (E-F).

The results discussed so far were obtained by employing electrodes with average nanowire length around 4 µm. Irrespective of the implemented thermal treatment, all these electrodes were produced by nickel electrodeposition in alumina templates generated by 2 hours aluminium anodization. On the other hand, the nanowire length can be easily modified with the implemented synthesis by varying the duration of the aluminium anodization: increasing the duration of aluminium anodization will result in alumina templates with longer nanopores, which will allow electrodepositing longer nanowires. The influence of the nanowire length was analysed by employing only electrodes of the type NiNW70, which were found to exhibit optimal thickness and composition of the active phase layer. Figure 6 shows the SEM cross-sectional images of the NiNW70 electrodes synthesized by electrodeposition into the pores of alumina templates produced by 2, 3, 4, 8, 10 h aluminium anodizations. The evolutions of the alumina pore length and of the nanowire length with the anodization time are reported in Fig.7A. It is important to notice that the nanowire length is not uniform across the array and the reported nanowire lengths are average values derived from SEM images. In accordance with Fig.7A, the alumina pore length provides a fair estimation for the average length of the nanowires up to 3 µm pore length (4 h anodization). However, deviations are found, starting from around 4 µm pore length, between the alumina pore length and the average nanowire length, which progressively increase with increasing the pore length. The main motivation behind this deviation is that increasing the alumina pore length increases the heterogeneity of the nanowire length distribution. SEM images reported in

Fig. 6 indicate that increasing the nanowire length increases the probability of nanowire breaking, which causes the appearance of contiguous nanowire arrays characterized by different lengths (see low-magnification images in Fig.6F). NiNW70 electrodes with different nanowire lengths were tested by galvanostatic cycling experiments. Figure 7B reports the potential profiles recorded during galvanostatic cycling. The increase in the nanowires length determines an increase in the loading of the electroactive material per geometric surface area and thus it is expected to increase the charge-discharge time. This prediction is consistent with the galvanostatic cycles recorded at current densities of 2.5 and 20 mA/cm2 (Figs.7B-C) with only one statistically significant exception: the electrode capacitance decreases with increasing the nanowire length from 17 to 21 μm at 2.5 mA cm^{-2} (Fig. 7B). This may be attributed to the increased number of nanowire breakings found with increasing the average nanowire length that probably also justifies the voltage drop difference between these two electrodes.

Electrode capacitance values computed by using Eq.5 are reported in Fig.7D. The capacitance increases with increasing the nanowire length, which can be explained by the active material loading increasing with the length, and it decreases with increasing the current density owing to the occurrence of mass transfer

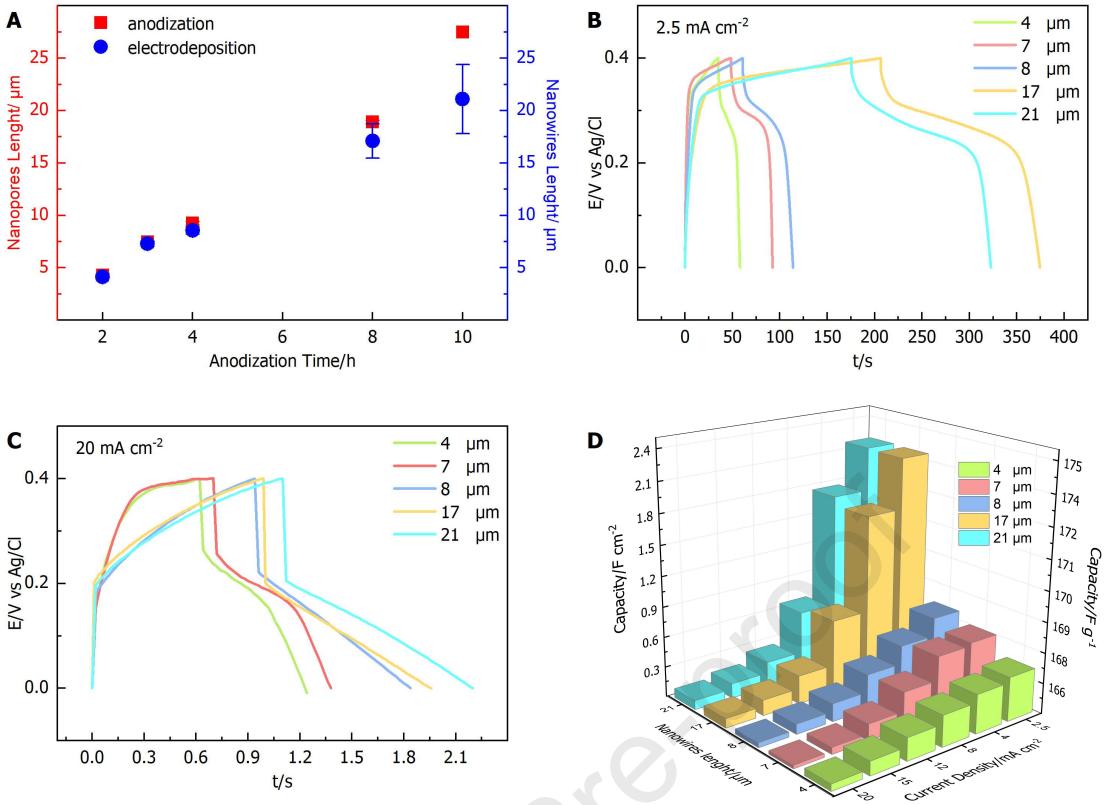

Figure 7: A) obtained nanowires length for different aluminium anodization time. Charge–discharge curves at 2.5 mA cm^{-2} (B) and 20 mA cm^{-2} (C) for different nanowires length of the electrodes. D) Capacitance values for the different electrodes and current densities.

limitations. It must be remarked that the specific capacitance values were computed considering the whole nanowires-based electrodes including the inactive metallic core and the thin nickel film current collector weights.

However, increasing the nanowire length can increase the resistance to ion transport (e.g. OH^- needed for NiO charging) through the electrolyte solution and thus the nanowire sections closer to the current collector may provide a contribution to the capacitance lower than the upper nanowire sections, which are closer to the bulk solution. This implies that successive identical increments in the nanowire length may produce contributions to capacitance progressively decreasing with the length. Capacitance values reported in Fig.7D are normalized by the geometric surface area, which is identical for any electrode irrespective of the length, and thus they cannot quantify how successive increments in the nanowire length contribute to increase the electrode capacitance. To this purpose, the electrode capacitance values normalized by the length were

computed and reported in Fig.8A.

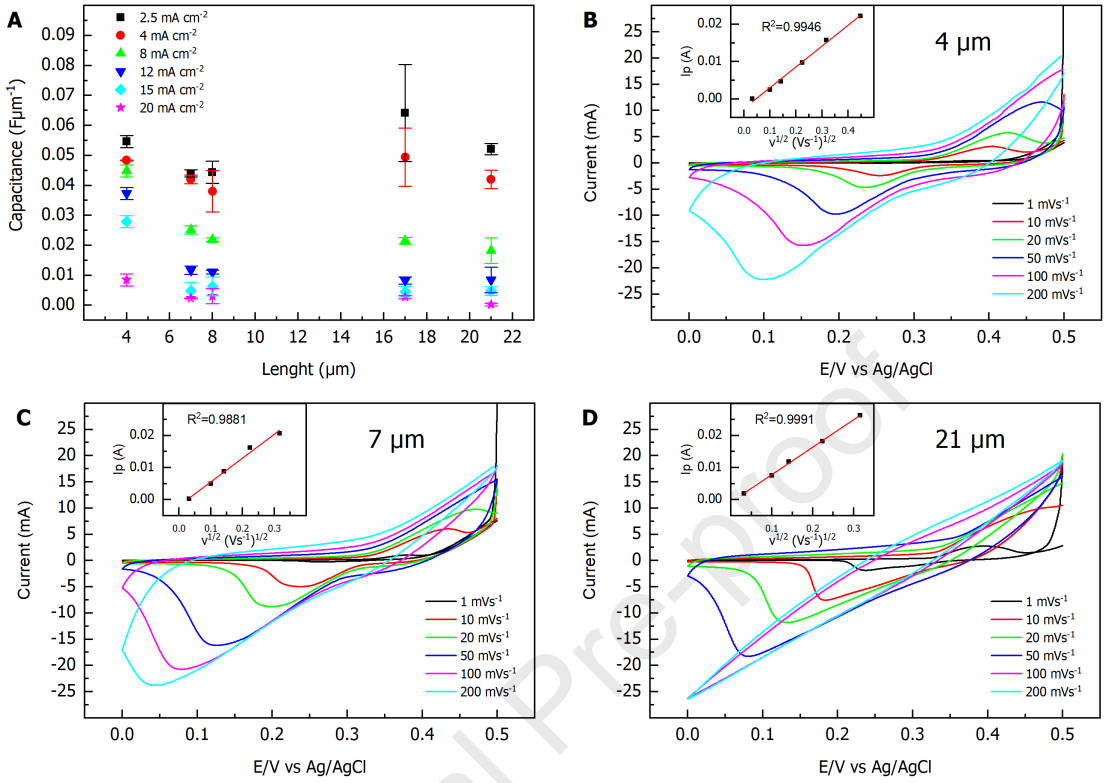

Figure 8. A) Capacitance values normalized per nanowires length. Cyclic voltammetry performed at different scan rate of electrode with nanowires length of 4 (B), 7 (C) and 21 (D) μm. Inset graph report the linear trend between cathodic peak current and the square root of scan rates

At any current density, the capacitance per length unit slightly decreases as the nanowire length increases from 4 to 5 μm and then remains nearly constant (i.e. absence of statistically significant variations) with increasing the nanowire length up to 21 μm. The constant capacitance per length unit attained between 5 and 21 μm indicates that any section of the synthesized 21 μm nanowire electrode provides an identical contribution to the capacitance and thus it can be advantageous to further increase the capacitance by increasing the nanowire length above 21 μm. This implies that the resistance to mass transfer in the electrolyte solution wetting the nanowires is negligible over the selected nanowire length interval. In this latter interval, the rate of nanowire charging and discharging is mainly dictated by the proton and hydroxyl diffusion. This is confirmed by the analysis of the cyclic voltammetries reported in Figs. 8B-D for the 4, 7 and 21 μm electrodes at scan rate ranging from 1 to 200 mV s^{-1}. The current density at the cathodic peak varies

linearly with the square root of the scan rate, indicating that the charging process becomes, at sufficiently cathodic potentials, limited by diffusion.

4. Conclusions

The influence of thermal treatment and nanowire length on the performance of nickel nanowires electrodes was reported. The thermal treatment at 40, 70 and 300°C has highlighted the key role played by the presence of a Ni metallic core for the obtainment of high conductivity electrodes, ensuring low charge transfer resistance and a corresponding high recorded capacitance. Annealing the electrode at 300 °C led to the conversion of Ni nanowires to NiO, while the thermal treatment at 40 and 70°C allowed for a tuning of the electroactive phase composition, preserving the metallic Ni core of the nanowires. For these latter electrodes the capacitance increased with the temperature of the thermal treatment, while the capacitance dropped to a minimum for the electrode annealed at 300°C. The higher capacitance attained by decreasing the $Ni(OH)_2$/NiO ratio upon heating at 70 °C can be explained by the different charge storage mechanisms for $Ni(OH)_2$ and NiO. $Ni(OH)_2$ involves the intercalation and diffusion of H^+ through the bulk active material, while NiO reacts with OH^- over the active site onto the nanowires surface. The proposed electrochemical method for the synthesis of nanowires-based electrode has allowed for a tuning of nanowires length by simple increasing the anodization time for the template production. A constant capacitance per nanowires length unit was attained varying the nanowires length between 5 and 21 μm, indicating that the resistance to mass transfer in the electrolyte solution is negligible in this range. The obtainment of electrodes with a controlled nanowires length opens the possibility to evaluate the presence of limiting mass transfer process on the capacitance. For all the investigated nanowires lengths, the current density at the cathodic peak, recorded during the cyclic voltammetries, varies linearly with the square root of the scan rate, indicating that the charging process is governed by proton and hydroxyl diffusion. The reported results have shown as the control of the thickness and the composition of the active phase shell, together with an optimal nanowires length, are pivotal to optimize the electrode performances of core-shell nanowires electrodes. This result could provide a guideline to optimize the capacitance of devices based on core-shell electrodes and sheds light on the possibility to tailor the capacity by tuning the material loading per geometric surface area, an aspect generally lacking in the literature. Future studies should be aimed at further clarifying how the phase ratio NiO/$Ni(OH)_2$ and the distribution of the two phases (NiO and $Ni(OH)_2$) through the electrode can

influence the electrochemical performances. To this purpose, mathematical models simultaneously describing the diffusion of protons through the composite and the reaction of hydroxyl ions at the active sites of the surface NiO phase should be validated based on the reported experimental results and thoroughly simulated.

5. References

[1] P. Simon, Y. Gogotsi, B. Dunn, Where do batteries end and supercapacitors begin?, Science, 343 (2014) 1210-1211.
[2] D. Chen, Q. Wang, R. Wang, G. Shen, Ternary oxide nanostructured materials for supercapacitors: a review, Journal of Materials Chemistry A, 3 (2015) 10158-10173.
[3] K.-C. Ho, L.-Y. Lin, A review of electrode materials based on core–shell nanostructures for electrochemical supercapacitors, Journal of materials chemistry A, 7 (2019) 3516-3530.
[4] Z. Liang, R. Zhao, T. Qiu, R. Zou, Q. Xu, Metal-organic framework-derived materials for electrochemical energy applications, EnergyChem, 1 (2019) 100001.
[5] E. Mourad, L. Coustan, P. Lannelongue, D. Zigah, A. Mehdi, A. Vioux, S.A. Freunberger, F. Favier, O. Fontaine, Biredox ionic liquids with solid-like redox density in the liquid state for high-energy supercapacitors, Nature materials, 16 (2017) 446-453.
[6] K. Krishnamoorthy, P. Pazhamalai, S. Sahoo, J.H. Lim, K.H. Choi, S.J. Kim, A High-Energy Aqueous Sodium-Ion Capacitor with Nickel Hexacyanoferrate and Graphene Electrodes, 4 (2017) 3302-3308.
[7] K.-J. Huang, J.-Z. Zhang, J.-L. Cai, Preparation of porous layered molybdenum selenide-graphene composites on Ni foam for high-performance supercapacitor and electrochemical sensing, Electrochim. Acta, 180 (2015) 770-777.
[8] C. Xiong, T. Li, A. Dang, T. Zhao, H. Li, H. Lv, Two-step approach of fabrication of three-dimensional MnO2-graphene-carbon nanotube hybrid as a binder-free supercapacitor electrode, J. Power Sources, 306 (2016) 602-610.
[9] B. Li, M. Zheng, H. Xue, H. Pang, High performance electrochemical capacitor materials focusing on nickel based materials, Inorganic Chemistry Frontiers, 3 (2016) 175-202.
[10] Q. Li, S. Zheng, Y. Xu, H. Xue, H. Pang, Ruthenium based materials as electrode materials for supercapacitors, Chem. Eng. J., 333 (2018) 505-518.
[11] S. Korkmaz, F.M. Tezel, İ. Kariper, Synthesis and characterization of GO/IrO2 thin film supercapacitor, J. Alloys Compd., 754 (2018) 14-25.
[12] S. Makino, Y. Yamauchi, W. Sugimoto, Synthesis of electro-deposited ordered mesoporous RuOx using lyotropic liquid crystal and application toward micro-supercapacitors, J. Power Sources, 227 (2013) 153-160.
[13] T. Wang, H.C. Chen, F. Yu, X.S. Zhao, H. Wang, Boosting the cycling stability of transition metal compounds-based supercapacitors, Energy Storage Materials, 16 (2019) 545-573.
[14] M. Zhao, Q. Zhao, B. Li, H. Xue, H. Pang, C. Chen, Recent progress in layered double hydroxide based materials for electrochemical capacitors: design, synthesis and performance, Nanoscale, 9 (2017) 15206-15225.
[15] J. Kang, S. Zhang, Z. Zhang, Three-dimensional binder-free nanoarchitectures for advanced pseudocapacitors, Adv. Mater., 29 (2017) 1700515.
[16] X. Long, Z. Wang, S. Xiao, Y. An, S. Yang, Transition metal based layered double hydroxides tailored for energy conversion and storage, Mater. Today, 19 (2016) 213-226.
[17] X. Xiao, L. Zou, H. Pang, Q. Xu, Synthesis of micro/nanoscaled metal–organic frameworks and their direct electrochemical applications, Chem. Soc. Rev., 49 (2020) 301-331.

[18] X. Li, X. Yang, H. Xue, H. Pang, Q. Xu, Metal–organic frameworks as a platform for clean energy applications, EnergyChem, 2 (2020) 100027.
[19] S. Zheng, Q. Li, H. Xue, H. Pang, Q. Xu, A highly alkaline-stable metal oxide@ metal–organic framework composite for high-performance electrochemical energy storage, National Science Review, 7 (2020) 305-314.
[20] L. Zhang, D. Shi, T. Liu, M. Jaroniec, J.J.M.T. Yu, Nickel-based materials for supercapacitors, 25 (2019) 35-65.
[21] U.K. Chime, A.C. Nkele, S. Ezugwu, A.C. Nwanya, N.M. Shinde, M. Kabede, P.M. Ejikeme, M. Maaza, F.I. Ezema, Recent Progress in Nickel Oxide-Based Electrodes for High-Performance Supercapacitors, Current Opinion in Electrochemistry, (2020).
[22] A.-L. Brisse, P. Stevens, G. Toussaint, O. Crosnier, T. Brousse, Ni (OH) 2 and NiO based composites: battery type electrode materials for hybrid supercapacitor devices, Materials, 11 (2018) 1178.
[23] L. Zhang, D. Shi, T. Liu, M. Jaroniec, J. Yu, Nickel-based materials for supercapacitors, Mater. Today, 25 (2019) 35-65.
[24] J. Zhao, Y. Tian, A. Liu, L. Song, Z. Zhao, The NiO electrode materials in electrochemical capacitor: A review, Mater. Sci. Semicond. Process., 96 (2019) 78-90.
[25] X. Liu, J. Wang, G. Yang, Amorphous nickel oxide and crystalline manganese oxide nanocomposite electrode for transparent and flexible supercapacitor, Chem. Eng. J., 347 (2018) 101-110.
[26] B. Dong, M. Li, S. Chen, D. Ding, W. Wei, G. Gao, S. Ding, Formation of g-C3N4@Ni(OH)2 Honeycomb Nanostructure and Asymmetric Supercapacitor with High Energy and Power Density, ACS Applied Materials and Interfaces, 9 (2017) 17890-17896.
[27] D. He, G. Liu, A. Pang, Y. Jiang, H. Suo, C. Zhao, A high-performance supercapacitor electrode based on tremella-like NiC2O4@NiO core/shell hierarchical nanostructures on nickel foam, Dalton Transactions, 46 (2017) 1857-1863.
[28] L. Hou, W. Yang, R. Li, X. Xu, P. Wang, B. Deng, F. Yang, Y. Li, Self-reconstruction strategy to synthesis of Ni/Co-OOH nanoflowers decorated with N, S co-doped carbon for high-performance energy storage, Chem. Eng. J., (2020) 125323.
[29] J.-Q. Xie, L. Jiang, J. Chen, D. Mao, Y. Ji, X.-Z. Fu, R. Sun, C.-P. Wong, Ni-Mn hydroxides supported on porous Ni/graphene films as high electrically and thermally conductive electrodes for supercapacitors, Chem. Eng. J., (2020) 124598.
[30] Y. Li, J. Henzie, T. Park, J. Wang, C. Young, H. Xie, J.W. Yi, J. Li, M. Kim, J. Kim, Fabrication of flexible microsupercapacitors with binder-free ZIF-8 derived carbon films via electrophoretic deposition, Bull. Chem. Soc. Jpn., 93 (2020) 176-181.
[31] W. Guo, C. Yu, S. Li, Z. Wang, J. Yu, H. Huang, J. Qiu, Strategies and insights towards the intrinsic capacitive properties of MnO2 for supercapacitors: challenges and perspectives, Nano Energy, 57 (2019) 459-472.
[32] S. Li, C. Yu, J. Yang, C. Zhao, M. Zhang, H. Huang, Z. Liu, W. Guo, J. Qiu, A superhydrophilic "nanoglue" for stabilizing metal hydroxides onto carbon materials for high-energy and ultralong-life asymmetric supercapacitors, Energy & Environmental Science, 10 (2017) 1958-1965.
[33] W. Guo, C. Yu, S. Li, X. Song, H. Huang, X. Han, Z. Wang, Z. Liu, J. Yu, X. Tan, A Universal Converse Voltage Process for Triggering Transition Metal Hybrids In Situ Phase Restruction toward Ultrahigh-Rate Supercapacitors, Adv. Mater., 31 (2019) 1901241.
[34] S.U. Muhamad, N.H. Idris, H.M. Yusoff, M.F.M. Din, S.R. Majid, In-situ encapsulation of nickel nanoparticles in polypyrrole nanofibres with enhanced performance for supercapacitor, Electrochim. Acta, 249 (2017) 9-15.
[35] X. Shi, J. Key, S. Ji, V. Linkov, F. Liu, H. Wang, H. Gai, R. Wang, Ni (OH) 2 nanoflakes supported on 3D Ni3Se2 nanowire array as highly efficient electrodes for asymmetric supercapacitor and Ni/MH battery, Small, 15 (2019) 1802861.
[36] N.L.W. Septiani, Y.V. Kaneti, K.B. Fathoni, J. Wang, Y. Ide, B. Yuliarto, H.K. Dipojono, A.K. Nanjundan, D. Golberg, Y. Bando, Self-assembly of nickel phosphate-based nanotubes into two-

dimensional crumpled sheet-like architectures for high-performance asymmetric supercapacitors, Nano Energy, 67 (2020) 104270.
[37] H. Sun, Z. Ma, Y. Qiu, H. Liu, G.g. Gao, Ni@ NiO nanowires on nickel foam prepared via "acid hungry" strategy: high supercapacitor performance and robust electrocatalysts for water splitting reaction, Small, 14 (2018) 1800294.
[38] L. Wang, H. Wang, C. Qing, G. Qu, W. Ma, Y. Tang, Controllable shell thickness of Co/CoO core-shell structure on 3D nickel foam with high performance supercapacitors, J. Alloys Compd., 726 (2017) 139-147.
[39] S. Xu, X. Li, Z. Yang, T. Wang, W. Jiang, C. Yang, S. Wang, N. Hu, H. Wei, Y. Zhang, Nanofoaming to Boost the Electrochemical Performance of Ni@Ni(OH)2 Nanowires for Ultrahigh Volumetric Supercapacitors, ACS Applied Materials & Interfaces, 8 (2016) 27868-27876.
[40] M. Hasan, M. Jamal, K.M. Razeeb, Coaxial NiO/Ni nanowire arrays for high performance pseudocapacitor applications, Electrochim. Acta, 60 (2012) 193-200.
[41] K. Yu, X. Pan, G. Zhang, X. Liao, X. Zhou, M. Yan, L. Xu, L. Mai, Nanowires in Energy Storage Devices: Structures, Synthesis, and Applications, Advanced Energy Materials, 8 (2018) 1802369.
[42] V. Srinivasan, J.W. Weidner, Studies on the capacitance of nickel oxide films: effect of heating temperature and electrolyte concentration, J. Electrochem. Soc., 147 (2000) 880-885.
[43] B.K. Kim, V. Chabot, A. Yu, Carbon nanomaterials supported Ni (OH) 2/NiO hybrid flower structure for supercapacitor, Electrochim. Acta, 109 (2013) 370-380.
[44] P.G. Schiavi, L. Farina, P. Altimari, M.A. Navarra, R. Zanoni, S. Panero, F. Pagnanelli, A versatile electrochemical method to synthesize Co-CoO core-shell nanowires anodes for lithium ion batteries with superior stability and rate capability, Electrochim. Acta, 290 (2018) 347-355.
[45] P.G. Schiavi, L. Farina, R. Zanoni, P. Altimari, I. Cojocariu, A. Rubino, M.A. Navarra, S. Panero, F. Pagnanelli, Electrochemical synthesis of nanowire anodes from spent lithium ion batteries, Electrochim. Acta, 319 (2019) 481-489.
[46] J.H. Scofield, Hartree-Slater subshell photoionization cross-sections at 1254 and 1487 eV, J. Electron. Spectrosc. Relat. Phenom., 8 (1976) 129-137.
[47] D. Briggs, Practical surface analysis, Auger and X-Ray Photoelecton Spectroscory, 1 (1990) 151-152.
[48] J. Vanpaemel, M.H. van der Veen, S. De Gendt, P.M. Vereecken, Enhanced nucleation of Ni nanoparticles on TiN through H3BO3-mediated growth inhibition, Electrochim. Acta, 109 (2013) 411-418.
[49] P.G. Schiavi, P. Altimari, R. Zanoni, F. Pagnanelli, Morphology-controlled synthesis of cobalt nanostructures by facile electrodeposition: transition from hexagonal nanoplatelets to nanoflakes, Electrochim. Acta, 220 (2016) 405-416.
[50] L.A. Hutton, M. Vidotti, A.N. Patel, M.E. Newton, P.R. Unwin, J.V.J.T.J.o.P.C.C. Macpherson, Electrodeposition of nickel hydroxide nanoparticles on boron-doped diamond electrodes for oxidative electrocatalysis, 115 (2010) 1649-1658.
[51] S. Tanuma, C.J. Powell, D.R. Penn, Calculations of electron inelastic mean free paths. IX. Data for 41 elemental solids over the 50 eV to 30 keV range, Surf. Interface Anal., 43 (2011) 689-713.
[52] A.G. Marrani, V. Novelli, S. Sheehan, D.P. Dowling, D. Dini, Probing the Redox States at the Surface of Electroactive Nanoporous NiO Thin Films, ACS Applied Materials & Interfaces, 6 (2014) 143-152.
[53] M.C. Biesinger, B.P. Payne, A.P. Grosvenor, L.W. Lau, A.R. Gerson, R.S.C. Smart, Resolving surface chemical states in XPS analysis of first row transition metals, oxides and hydroxides: Cr, Mn, Fe, Co and Ni, Appl. Surf. Sci., 257 (2011) 2717-2730.
[54] M.-S. Wu, H.-H. Hsieh, Nickel oxide/hydroxide nanoplatelets synthesized by chemical precipitation for electrochemical capacitors, Electrochim. Acta, 53 (2008) 3427-3435.
[55] X. Liu, J. Jiang, L. Ai, Non-precious cobalt oxalate microstructures as highly efficient electrocatalysts for oxygen evolution reaction, Journal of Materials Chemistry A, 3 (2015) 9707-9713.

[56] P.T. Babar, A.C. Lokhande, M.G. Gang, B.S. Pawar, S.M. Pawar, J.H. Kim, Thermally oxidized porous NiO as an efficient oxygen evolution reaction (OER) electrocatalyst for electrochemical water splitting application, Journal of industrial and engineering chemistry, 60 (2018) 493-497.
[57] Y. Wang, L. Huang, L. Ai, M. Wang, Z. Fan, J. Jiang, H. Sun, S. Wang, Ultrathin nickel-cobalt inorganic-organic hydroxide hybrid nanobelts as highly efficient electrocatalysts for oxygen evolution reaction, Electrochim. Acta, 318 (2019) 966-976.
[58] C. Zhou, J. Mu, Y.-F. Qi, Q. Wang, X.-J. Zhao, E.-C. Yang, Iron-substituted Co-Ni phosphides immobilized on Ni foam as efficient self-supported 3D hierarchical electrocatalysts for oxygen evolution reaction, Int. J. Hydrogen Energy, 44 (2019) 8156-8165.
[59] S. Vijayakumar, S. Nagamuthu, G. Muralidharan, Supercapacitor Studies on NiO Nanoflakes Synthesized Through a Microwave Route, ACS Applied Materials & Interfaces, 5 (2013) 2188-2196.
[60] M. Ghaemi, F. Ataherian, A. Zolfaghari, S.M. Jafari, Charge storage mechanism of sonochemically prepared MnO2 as supercapacitor electrode: Effects of physisorbed water and proton conduction, Electrochim. Acta, 53 (2008) 4607-4614.
[61] V. Srinivasan, J.W. Weidner, R.E. White, Mathematical models of the nickel hydroxide active material, J. Solid State Electrochem., 4 (2000) 367-382.
[62] M. Khairy, S.A. El-Safty, Mesoporous NiO nanoarchitectures for electrochemical energy storage: influence of size, porosity, and morphology, RSC Advances, 3 (2013) 23801-23809.
[63] K.P. Ta, J.J.J.o.t.E.S. Newman, Mass transfer and kinetic phenomena at the nickel hydroxide electrode, 145 (1998) 3860.
[64] Y. Zhao, X. Li, B. Yan, D. Li, S. Lawes, X. Sun, Significant impact of 2D graphene nanosheets on large volume change tin-based anodes in lithium-ion batteries: a review, J. Power Sources, 274 (2015) 869-884.
[65] L. Zhan, S. Wang, L.-X. Ding, Z. Li, H. Wang, Grass-like Co3O4 nanowire arrays anode with high rate capability and excellent cycling stability for lithium-ion batteries, Electrochim. Acta, 135 (2014) 35-41.

- The role of metallic core, $Ni(OH)_2$/NiO ratio and nanowire length was investigated
- Capacitance increase lowering $Ni(OH)_2$/NiO ratio of the active phase shell
- Lack of Ni(0) core leads to an increase of resistance and a lower capacitance
- A constant capacitance per nanowires length unit was attained between 5 and 21 μm

Declaration of interests

☒ The authors declare that they have no known competing financial interests or personal relationships that could have appeared to influence the work reported in this paper.

☐The authors declare the following financial interests/personal relationships which may be considered as potential competing interests: